AGU PUBLICATIONS

JGR

Journal of Geophysical Research: Space Physics

RESEARCH ARTICLE

10.1002/2013JA019241

Key Points:
- Routine detection of meteor head echoes using a meteor radar
- A new technique to perform continuous and detail measurements of meteoroids
- Link directly atmospheric processes with particle orbital characteristics

Correspondence to:
D. Janches,
diego.janches@nasa.gov

Citation:
Janches, D., W. Hocking, S. Pifko, J. L. Hormaechea, D. C. Fritts, C. Brunini, R. Michell, and M. Samara (2014), Interferometric meteor head echo observations using the Southern Argentina Agile Meteor Radar, *J. Geophys. Res. Space Physics*, *119*, doi:10.1002/2013JA019241.

Received 23 JUL 2013
Accepted 18 FEB 2014
Accepted article online 24 FEB 2014

Interferometric meteor head echo observations using the Southern Argentina Agile Meteor Radar

D. Janches[1], W. Hocking[2], S. Pifko[3], J. L. Hormaechea[4], D. C. Fritts[5], C. Brunini[6], R. Michell[7], and M. Samara[7]

[1]Space Weather Laboratory, NASA Goddard Space Flight Center, Greenbelt, Maryland, USA, [2]Department of Physics and Astronomy, University of Western Ontario, London, Ontario, Canada, [3]Department of Aeronautics and Astronautics, Stanford University, Stanford, California, USA, [4]Estacion Astronomica Rio Grande, Rio Grande, Tierra del Fuego, Argentina, [5]Gats Inc., Boulder, Colorado, USA, [6]Departamento de Ciencias Astronomicas y Geofisicas, Universidad Nacional de La Plata, La Plata, Argentina, [7]SouthWest Research Institute, San Antonio, Texas, USA

Abstract A radar meteor echo is the radar scattering signature from the free electrons generated by the entry of extraterrestrial particles into the atmosphere. Three categories of scattering mechanisms exist: specular, nonspecular trails, and head echoes. Generally, there are two types of radars utilized to detect meteors. Traditional VHF all-sky meteor radars primarily detect the specular trails, while high-power, large-aperture (HPLA) radars efficiently detect meteor head echoes and, in some cases, nonspecular trails. The fact that head echo measurements can be performed only with HPLA radars limits these studies in several ways. HPLA radars are sensitive instruments constraining the studies to the lower masses, and these observations cannot be performed continuously because they take place at national observatories with limited allocated observing time. These drawbacks can be addressed by developing head echo observing techniques with modified all-sky meteor radars. Such systems would also permit simultaneous detection of all different scattering mechanisms using the same instrument, rather than requiring assorted different classes of radars, which can help clarify observed differences between the different methodologies. In this study, we demonstrate that such concurrent observations are now possible, enabled by the enhanced design of the Southern Argentina Agile Meteor Radar (SAAMER). The results presented here are derived from observations performed over a period of 12 days in August 2011 and include meteoroid dynamical parameter distributions, radiants, and estimated masses. Overall, the SAAMER's head echo detections appear to be produced by larger particles than those which have been studied thus far using this technique.

1. Introduction

The collision of asteroids and disintegration of comets are the main source of dust in the solar system. These processes give rise to a thick circumsolar disk of small debris known as the Zodiacal Dust Cloud (ZDC). Several physical effects produced by larger solar system bodies result in the dust having relatively short lifetimes, maintaining a partial balance in their distribution and preventing this cloud from becoming dustier. For example, dust particles can be ejected from the solar system by Jupiter, thermally obliterated by the Sun, or physically fragmented by additional collisions among themselves. Also, a portion of the cloud is swept up by the planets, and for the case of those with atmospheres will produce the familiar phenomena of ionization and light production termed meteor. We now know that similar processes occur in other systems as circumstellar disks of dust have been observed, for example, around Beta Pitcoris [*Okamoto et al.*, 2004] and Formalhaut [*Currie et al.*, 2012]. Thus, studying the ZDC enables the understanding of its nature, shedding light into the history and development of the solar system as well as extra solar planetary environments [*Malhotra*, 1995; *Johansen et al.*, 2007; *Walsh et al.*, 2011; *Nesvorný et al.*, 2010; *Wiegert et al.*, 2009].

The ZDC is the source of meteoroids originating from the so-called sporadic meteor complex (SMC) formed by six apparent sources: Helion, Anti-Helion, North and South Apex, and North and South Toroidal [*Jones and Brown*, 1993, and reference therein]. The study of the ZDC, SMC, and their relation is fundamental for a number of areas of research within the solar system and planetary sciences realms and many basic questions regarding their nature still remain an unsolved puzzle [*Nesvorný et al.*, 2011b]. Issues of importance include the relative contribution of comets and asteroids to the overall dust budget, clarification of the dynamical processes that make particles of different sizes produce the observed light scattering and thermal

emissions, and the causes of the differences in relative strength of the sources [*Galligan and Baggaley*, 2005; *Campbell-Brown*, 2008a, 2008b; *Brown and Jones*, 1995; *Galligan and Baggaley*, 2005; *Nesvorný et al.*, 2010; *Wiegert et al.*, 2009]. In addition, the fact that knowledge of the ZDC can be utilized to estimate the amount of dust accreted by planets and satellites [*Nesvorný et al.*, 2010, 2011a] makes it a compelling tool for the additional study of the composition and chemistry of planetary atmospheres. The daily ablation of billions of interplanetary dust particles (IDPs) produces layers of neutral and ionized metal atoms in planetary atmospheres (e.g., ~ 90 km of altitude on Earth and Mars, ~120 km on Venus, and ~550 km on Titan) [*Plane*, 2003; *Pätzold et al.*, 2005, 2009; *Withers et al.*, 2008; *Kliore et al.*, 2008]. Once the meteoric metals are injected into the atmosphere, they are responsible for a diverse range of phenomena, including the following: the formation of layers of metal atoms and ions, nucleation of noctilucent clouds, impacts on stratospheric aerosols and O_3 chemistry, and fertilization of the ocean with bioavailable Fe, which has potential climate feedbacks [*Plane*, 2003].

Ground-based meteor observations with radars detect thousand of sporadic, as well as shower, events every day, providing data sets with excellent statistics and a variety of dynamical and physical information regarding the particles that produced the observed meteors. This makes radar meteor science an optimal tool to study the ZDC. The radar scattering signature produced by the interaction between the transmitted pulse and the ionized region generated by entry of extraterrestrial particles into the atmosphere gives rise to the radar meteor echo. Three categories of scattering mechanisms exist: specular trails, nonspecular trails, and head echoes. Generally, there are two types of radars utilized to detect meteors. Traditional VHF meteor radars (often called all-sky radars) primarily detect the specular reflection of meteor trails traveling perpendicular to the line of sight of the scattering trail while high-power, large-aperture (HPLA) radars efficiently detect meteor head echoes and, in some cases, nonspecular trails. Trails are generally semistationary echoes that originate from the ionization left behind by the meteoroid [*Baggaley*, 2002]. The specular or nonspecular nature of the trails depends on the viewing geometry and their position with respect to the magnetic field lines [*Dyrud et al.*, 2002]. While specular trails produce echoes that are confined to one altitude, nonspecular reflections occur from Field Align Instabilities that are spread in many range gates. Head echoes, on the other hand, are reflections from the plasma immediately surrounding the meteoroid itself traveling at, or near, its speed [*Janches et al.*, 2000a, 2003].

The first head echo detection was reported by *Hey et al.* [1947] who made observations with a 150 kW VHF radar system during the Giacobinid meteor storm of 1946, while *Evans* [1965] used the Millstone Hill incoherent scatter radar system to conduct the first head echo measurements using HPLA radars. However, routine operational worldwide head echo observations utilizing HPLA radar only began in earnest almost three decades later [*Pellinen-Wannberg and Wannberg*, 1994; *Mathews et al.*, 1997; *Close et al.*, 2000; *Sato et al.*, 2000; *Chau and Woodman*, 2004; *Janches et al.*, 2006; *Sparks et al.*, 2009]. Because head echoes allow direct detection of the meteoroid flight in the atmosphere, they provide information about meteoroid changes during the actual entry process and so provide key information for understanding mass loss mechanisms [*Kero et al.*, 2008; *Janches et al.*, 2009], electromagnetic plasma processes [*Dyrud et al.*, 2002], as well as enabling the quantification of the mass range of detected particles [*Close et al.*, 2012] and their effect in the upper atmosphere [*Fentzke and Janches*, 2008; *Gardner et al.*, 2011]. HPLA radars are characterized by their high peak transmitter power ($\geq$1 MW) at VHF and UHF frequencies that range between 50 and 1200 MHz, and antenna apertures, in the form of arrays or dishes, that have areas ranging between ~800 and 9×10^4 m^2 [*Janches et al.*, 2008] (see also section 5 and Table 2). This focuses most of the radiation into narrow beams with patterns characterized by full width at half maximum (FWHM) between 0.16 and 3°. In comparison, meteor radars generally transmit with a single Yagi or dipole antennas at VHF frequencies ranging from 17 to 50 MHz and peak power of the order of 6–20 kW [*Galligan and Baggaley*, 2004; *Brown et al.*, 2008; *Younger et al.*, 2009]. Thus, over the past decade, two distinct areas of research have developed separately in radar meteor science. The first one is based on the more classical detection of specular reflections of meteor trails using meteor radars, and the second is based on detection of head echoes and nonspecular trails utilizing HPLA radars. Results from both areas have shown significantly different observed meteoroid dynamical property distributions [*Janches et al.*, 2008] and trying to elucidate the origins of these differences has been challenging.

The fact that head echo measurements can be performed only with HPLA radars limits these studies in several ways. HPLA radars are very sensitive instruments with generally very narrow beam width. This constrain the studies to the lower masses within the spectrum of terrestrial atmospheric aeronomical interest

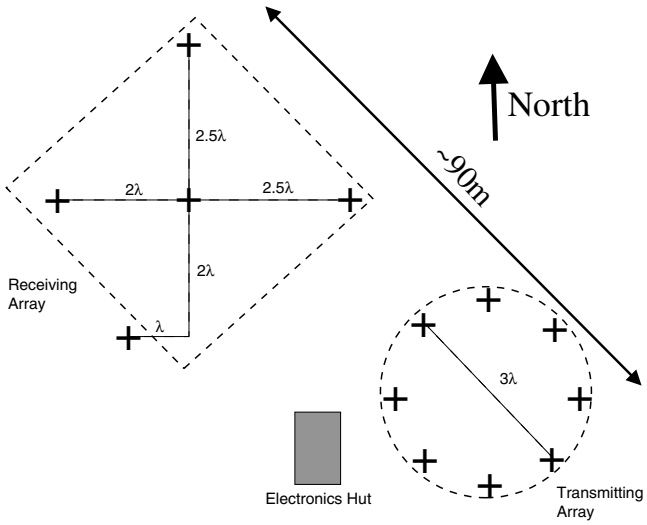

Figure 1. Antenna transmitter and receiver layout at Rio Grande, Tierra del Fuego (with individual antennas indicated with plus symbols).

[*Mathews et al.*, 2001]. HPLA radars can, in principle, detect particles with larger masses, but because the number of meteoroids decreases with increasing size, their probability that occur within the narrow beams decreases. In addition, meteor observations with HPLA radars are scarce because they are radars at national observatories, and as such, the allocated observing time in these instruments is limited. To date, only the Arecibo and the Middle and Upper (MU) radars have been used extensively to study seasonal effects in the observed meteor flux properties [*Janches et al.*, 2006; *Kero et al.*, 2011]. If head echo detections can successfully be made with meteor radars, such observations can potentially addresses these limitations. In addition, the fact that the detection of all different scattering mechanisms, only possible now using an assorted class of radars, can be made with the same instrument can contribute to the explanation of the observed differences. Thus, in this manuscript, we demonstrate that such observations are now possible with the Southern Argentina Agile Meteor Radar (SAAMER) enabled by its enhanced design. Section 2 discusses in detail the system characteristics while section 3 describes our data analysis methodology. In section 4, we present a summary of the most representative results and distributions from the head echo observations utilizing SAAMER, and compare them with past HPLA radar observations in section 5. In particular, we will compare our results with the Arecibo 430 MHz radar in Puerto Rico, the 440 MHz Poker Flat Incoherent Scatter Radar (PFISR) in Alaska, the 46 MHz Middle and Upper (MU) radar in Japan, the 160 MHz Advanced Research Project Agency Long-range Tracking and Instrumentation Radar (ALTAIR) in the Marshall Islands, and the 50 MHz Jicamarca radar in Peru.

2. SAAMER: System Description

SAAMER is a SKiYMET system [*Hocking et al.*, 1997] deployed at the Estacion Astronomica Rio Grande (EARG) in the city of Rio Grande (53.8°45′8″S; 67°45′5″W), province of Tierra del Fuego, Argentina. SAAMER has being operational continuously since May 2008 at a frequency of 32.55 MHz. It is enhanced relative to standard meteor radars, in order to enable Gravity Wave (GW) momentum flux measurements in the Mesosphere and Lower Thermosphere (MLT) atmospheric region [*Fritts et al.*, 2010a, 2010b]. These enhancements over the more traditional systems were driven by two important new requirements: (1) the need for significantly higher count rates and (2) a need for the majority of meteor detections to be at small zenith (high elevation) angles. Both needs were addressed with SAAMER, which additionally was designed for greatly enhanced transmitter peak power (60 kW, rather than 6–20 kW used by most meteor radar systems).

Of particular interest for this work, is that SAAMER uses a transmitter phase antenna array configuration, specially designed by Mardoc Inc., composed of eight 3-element crossed yagis arranged in an octagon of 27.6 m (three wavelengths) in diameter (Figure 1). This is significantly different from typical systems, which use a single antenna. In addition, the ability to change electronically (e.g., pulse to pulse) the

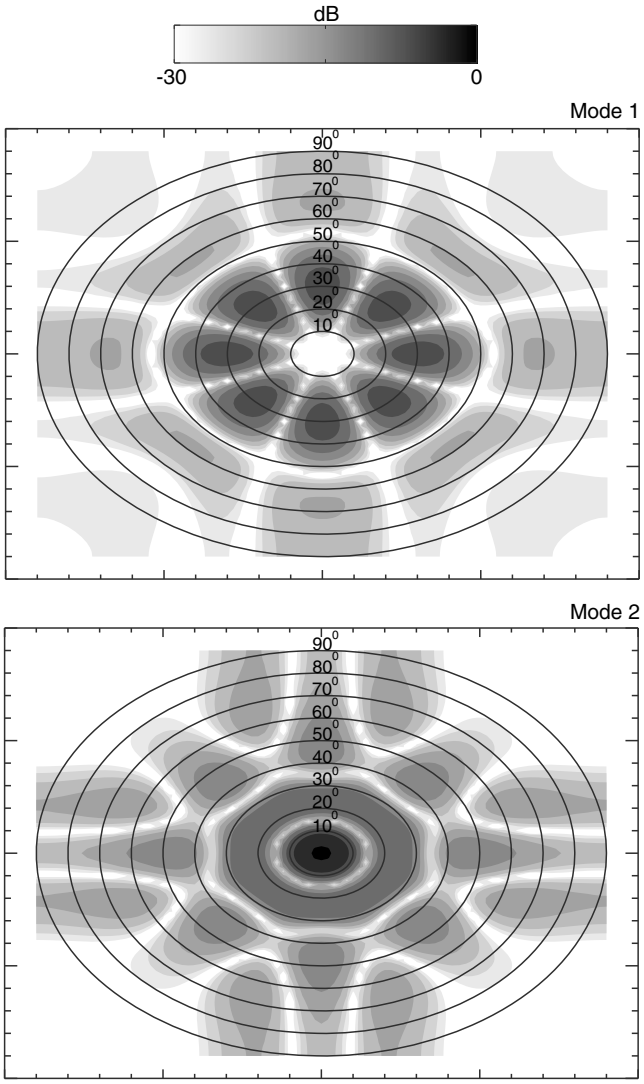

Figure 2. SAAMER's radiation patterns transmitting (a) Mode 1: 180° off phase and (b) Mode 2: all antennas in phase.

phases between antennas provides great flexibility to the system, since it allows transmission with different radiation patterns and hence permits performance of a number of different experiments. This makes SAAMER not only an operational instrument but also a system with which additional radar experiments can be implemented.

In the normal mode of operation (hereafter referred as Mode 1), designed to measure mesospheric winds, SAAMER transmits with opposite phasing of every other yagi, directing the majority of radar power into eight beams at 45° azimuth increments with peak power at ~35° off zenith (Figure 2a). This results in a majority of meteor specular trail detections at off-zenith angles between 15° and 50° [*Fritts et al.*, 2012a]. During the first 16 months of operation, SAAMER transmitted a 2 km (13.4 μs) long monopulse at 2140 Hz pulse repetition frequency (PRF) and a bandwidth of 0.3 MHz resulting in an excess of 10,000 meteor trail specular reflections detected daily. In September 2009, however, the transmitting scheme was changed to a 2-bit Barker code pulse of total length of 26.8 μs at a PRF of 1765 Hz. This change resulted in a ~40% increase in the daily counts, that is in 15,000 to 25,000 daily detected underdense specular meteor trail events [*Janches et al.*, 2013].

For the purpose of the work described herein, enabled by the agility of SAAMER's new transmitter design, we utilized a transmitting mode that somewhat follows the methodology applied in the past for meteor head echo observations utilizing HPLA radars (hereafter called Mode 2). As opposed to the semistationary

Table 1. SAAMER's Operating Characteristics for Head Echo Mode (Mode 2)

Quantity (Units)	
Latitude (degrees)	53.8°
Longitude (degrees)	67°
Frequency (MHz)	32.55
PRF (Hz)	500
Peak transmitted power (kW)	60
Bandwidth (MHz)	0.05
Coherent integrations (# of IPP)	2
Pulse code	Monopulse
Pulse length (μs)	13.6
Sampling resolution (m)	250
FWHM	8°

nature of specular reflections from meteor trails, the head echo originates from the plasma surrounding the meteoroid, moving at or near its speed [*Janches et al.*, 2000a]. Its radar cross section is much smaller than the trail [*Close et al.*, 2004], requiring far better detection sensitivity as well as improved temporal resolution. For these reasons, Mode 2 transmits with all the TX antennas in phase resulting in most of the radiated power upward in a relatively, narrow beam [*Janches et al.*, 2000b, 2002, 2003; *Sparks et al.*, 2009; *Pifko et al.*, 2013]. As displayed in Figure 2b, Mode 2 results in a near-Gaussian central transmitted beam pattern with a 3 dB decrease in gain at ~8°. We refer to this mode as a "relatively" narrow beam because when compared with HPLA systems, SAAMER's main beam width is approximately 3 times wider than the MU and ALTAIR radars [*Close et al.*, 2000; *Kero et al.*, 2011], 8 times wider than PFISR and Jicamarca [*Chau and Woodman*, 2004; *Sparks et al.*, 2010], and 50 times wider than the Arecibo radar [*Janches et al.*, 2004], yet is much narrower than the typical all-sky pattern resulting from a single yagi antenna utilized in most of the meteor radar systems [*Fritts et al.*, 2012a]. Specifically, we transmitted a 13.5 μs monopulse at a PRF of 500 Hz and performed a two-point pulse coherent integration, thus resulting in an effective Interpulse period (IPP) of 4 μs. The sampling resolution of the return signal was 250 m and the bandwidth was 0.05 MHz. The vertical altitude range covered was between ~75 km and 130 km. Table 1 presents a summary of SAAMER's operation characteristics in Mode 2. As it will be discussed in more detail in the following sections, the larger area and lower transmitted power, as compared to HPLA systems, will result in lower power density which will result in sensitivity to larger particles than those detected by HPLA radars. Hence, the ability to utilize SAAMER in head echo observing mode extends the size range of meteoroids for which this technique can be applied.

The data presented in this paper were obtained during an observing campaign performed between 2 and 14 August 2011. During that time, we also performed simultaneous optical observations that will be presented in a future paper. We transmitted in Mode 2 generally from evening hours until noon so as to cover the early morning meteor rate rise and peak [*Janches et al.*, 2006]. The return echoes are received by both the TX array and the receiving (RX) array, where the latter is formed by a modified version of the typical five antennas interferometer arrangement (Figure 1) [*Hocking et al.*, 1997], all of which are also three-element crossed yagis. Due to physical constrains at the location where SAAMER operates, the southernmost RX antenna was shifted off the cross axis toward the east by a distance equal to a wavelength (Figure 1). Such modification preserves all the characteristics of the interferometric antenna arrangement developed by *Hocking et al.* [1997] and demonstrates that the "cross" arrangement is just one of many antenna positioning options available to form a RX interferometer that enables redundant position definition of the detected echoes. For example, a clone system to SAAMER operating in the Brazilian Antarctic Base Comandate Ferraz in King George Island uses a "T" antenna arrangement [*Fritts et al.*, 2012b]. Using the interferometer, the position for each detected range gate at every IPP is determined with errors less than 0.5°, ultimately enabling the determination of absolute meteoroid velocities as discussed in the next section.

3. Data Analysis

SAAMER uses the basic real-time echo detection and analysis algorithms for the SKiYMET systems developed by *Hocking et al.* [2001], independently of what transmitting mode is been utilized. These algorithms simultaneously stream raw data into memory, detect occurrences of meteors, and identify and store those produced by underdense specular reflections [*McKinley*, 1961; *Ceplecha et al.*, 1998]. From these selected events, the location of meteor trails (range and angle) are determined, as well as their radial drift speeds and decay times. Underdense specular meteor trail events are semistationary targets drifting with the background wind at speeds that range typically from a few to ~100 m/s. Thus, when analyzing raw data, these events are detected in the same range gate during many IPPs until the returned signal strengths falls below the noise floor due to their diffusion in the background atmosphere [*Lau et al.*, 2006]. Head echoes, on the other hand, move at hypersonic speeds (~ km/s), and therefore, they will be detected over several range gates with increasing time (i.e., IPP) [*Janches et al.*, 2000a]. Thus, for the case of this work, additional data

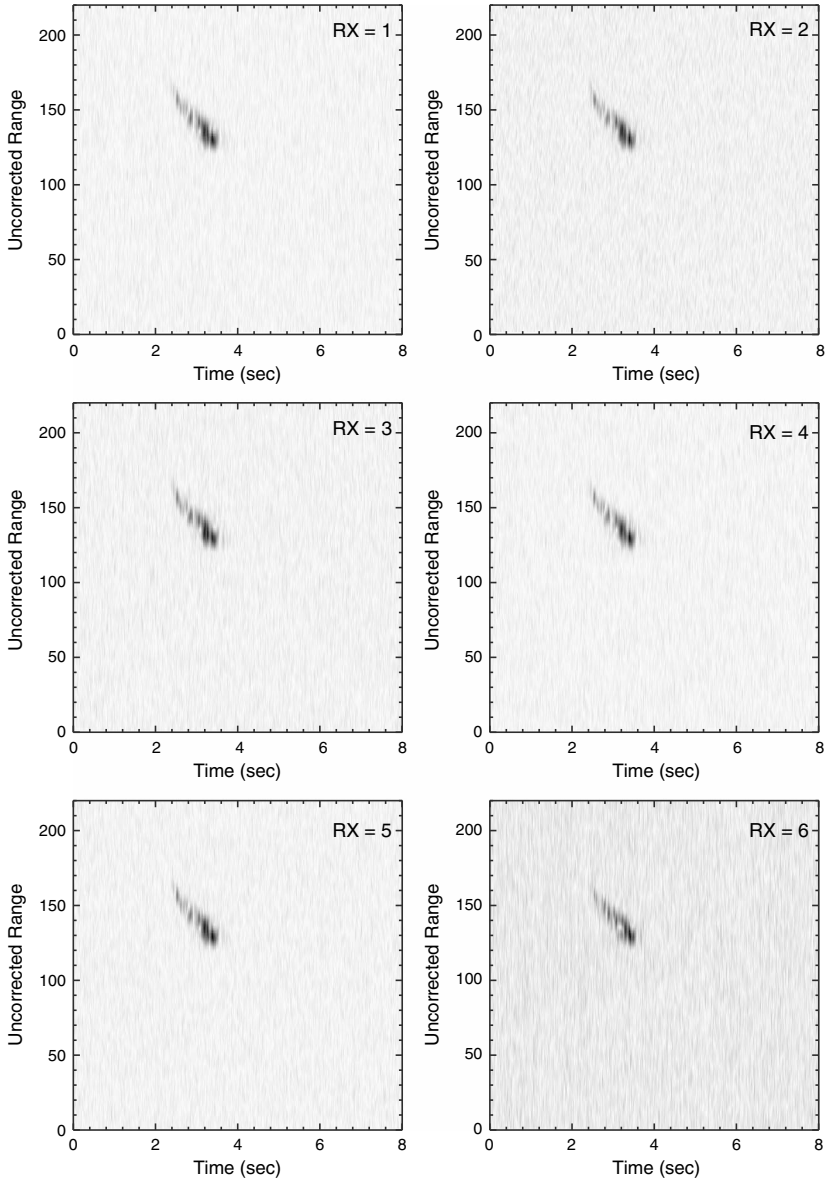

Figure 3. RTI Images of a head echo event observed by SAAMER. The first five panels represent the signal detected by each of the receiving antennas while the last panel displays the signal recorded by the transmitting array utilized as a receiver. Note this event also displays the beginning of a specular trail.

analysis and processing were required to be performed off-line. For this, we recorded the in-phase and quadrature components of the voltage of the returned signal for each range gate, coherently integrated over two IPPs for each of the six receiving channels, five from each of the antennas that form the RX array and one from the TX array used as a receiver. Initially, we performed a running average of the noise floor and searched through the raw data for enhancements greater than three sigmas above the noise. Due to the presence of thousands of trail events which are detected hourly by SAAMER, this simple approach is not efficient for identification of single head echoes, requiring that we perform a visual inspection among the detected candidates. Figures 3 and 4 show the Range-Time-Intensity (RTI) images for two examples of such events. The first five panels from each figure correspond to the data recorded on each of the RX array antenna. The sixth panel corresponds to data recorded with the eight-Yagi TX array utilized as a receiver. A common feature of the radars is that the echo return is range aliased and, for the case of meteor radars, the interferometric results as well as the assumption that meteors occur between 70 and 140 km of altitudes

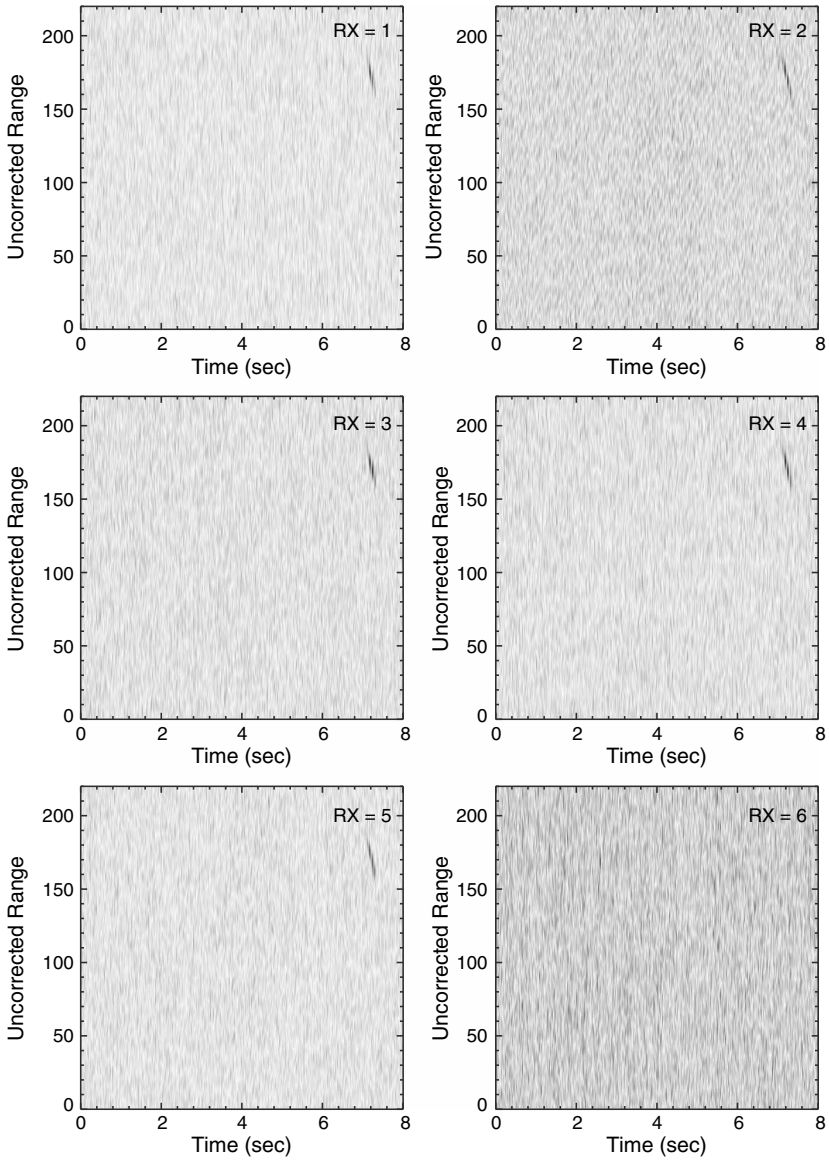

Figure 4. Same as Figure 3 for a second and much weaker-signal event.

are needed to obtain the corrected altitudes. This step is not yet applied for the data presented in Figures 3 and 4 and that is why the vertical axis show uncorrected ranges.

Once the head echo events had been identified, we proceeded to determine the meteoroid motion vector. For this, we performed interferometric calculations for every IPP by determining the phase differences between receiving channels for a selected range gate. As can be seen from the detailed RTI images displayed in Figure 5 of the two examples shown in Figures 3 and 4, for a given IPP, the events show a vertical spread of range gates which in many cases is longer than the pulse length. We then determine, for each IPP in which the meteor is present, the lowest range gate of the vertical signal range spread (i.e., leading edge) and select among 10 range gates (about the length of the pulse in ranges) from the lowest one, the gate with maximum signal strength. This is represented by the black dots in this figure. The use of the five antenna interferometer arrangement allows for the unambiguous determination of the spatial location for each IPP. This methodology is widely utilized and will not be described in this work. *Hocking et al.* [1997] and *Hocking et al.* [2001] described in detail the operation of the five antenna meteor radar interferometer. The application of interferometry for head echo purposes has been reported by *Sato et al.* [2000], *Chau and Woodman* [2004], *Hunt et al.* [2004], and *Sparks et al.* [2010]. The results of the interferometry calculation for

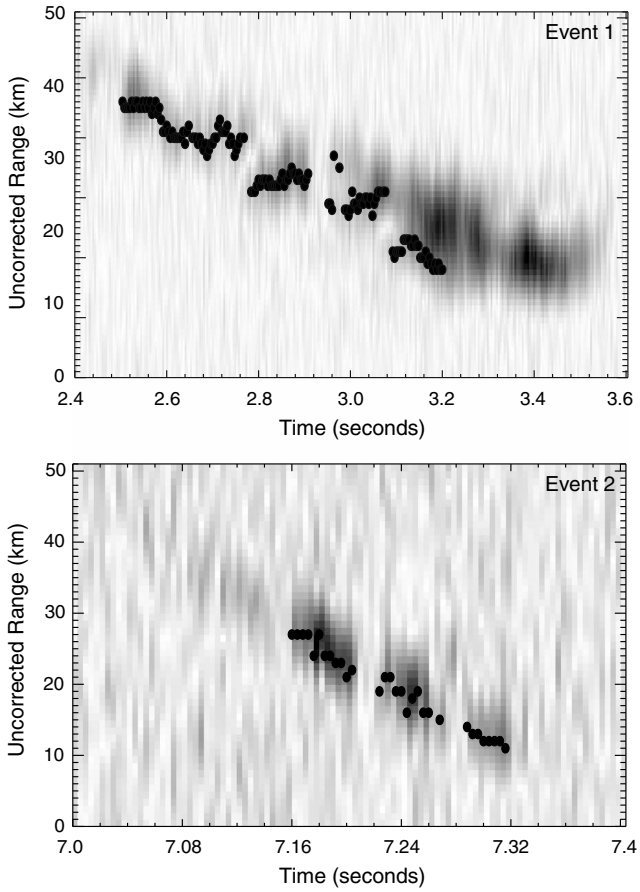

Figure 5. Detail RTI images of the events displayed in Figures 3 and 4. The black dots show the range gates that were utilized for interferometric calculation purposes.

both examples are displayed in Figure 6 where the vertical, eastward, and northward positions for each IPP are shown as black dots. It is evident from these panels that the interferometric results are noisier than those reported in the past by HPLA radars [*Sparks et al.*, 2010, and reference therein]. However, a clear trend is present in the data and a linear fits can be applied in order to obtain an estimate of each component of the vector velocity. An interesting point to note from these panels is that both events were detected at heights greater than 110 km, somewhat greater than average altitudes reported in previous HPLA observations (~105 km) [*Janches et al.*, 2002, 2003; *Sparks et al.*, 2009; *Pifko et al.*, 2013]. In addition, the distance traveled in some of the planes, in some cases greater than 10 km, are relatively larger than previous HPLA observations. Although some dependency on the lower transmitted frequency and radar beam size exists, both factors also suggest that these head echoes are produced by relatively larger particles than those detected by HPLA systems [*Janches et al.*, 2008; *Pifko et al.*, 2013]. In the next section, we present a summary of the results obtained throughout the observing campaign.

4. Results

As described in section 2, the data presented in this work were obtained over a period of 12 days covering 2 to 14 August 2011. Due to the low sensitivity of SAAMER, we did not expect meteor head echo detection rates to be as large as is the case for HPLA radars (>10 events/min at the peak). In addition, because these observations were performed simultaneously with an optical campaign aimed at observing the same events with radar and optical techniques, we concentrated mostly on night hours, with the inclusion of mornings to cover the flux rate increase and peaks [*Janches et al.*, 2006], thus increasing the likelihood of successful observations. Figure 7 displays the observing interval times for each day of observations. Figure 8 provides information on the head echo detection rate observed by SAAMER. Over the 12 days of observations, an average of ~15 head echoes where observed (Figure 8a) during each observing period that lasted on

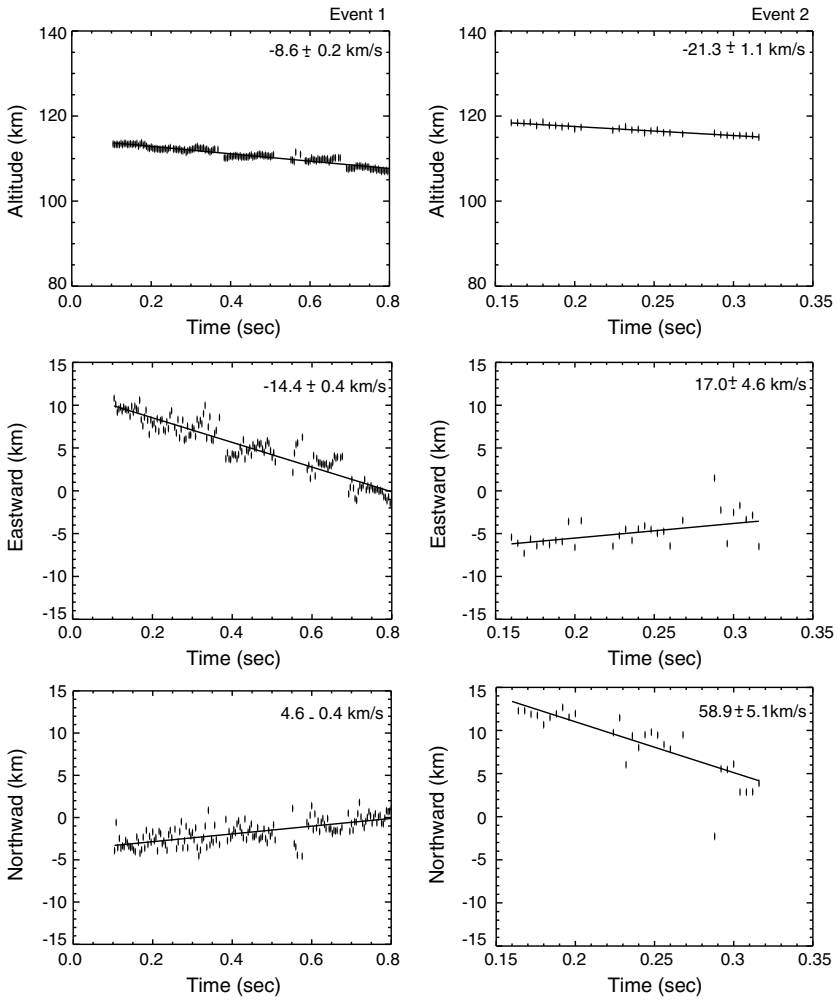

Figure 6. Interferometric spatial and velocity determinations of the events displayed in Figures 3 and 4.

average ~14 h (Figure 8b), resulting in, approximately, one detection every hour (Figure 8c). Figure 8d displays the number of head echoes detected through out the day for all the days combined. Although observations were stopped after local noon (Figure 7), Figure 8d indicates that most of the detections occur between 5 A.M. and noon, consistent with the diurnal behavior of meteor head echoes observed by HPLA radars [*Janches et al.*, 2006; *Fentzke et al.*, 2009; *Sparks et al.*, 2009]. As can be derived from Figure 8, the SAAMER head echo detection rate is up to 2 order of magnitude lower than those resulting from HPLA radar observations [*Janches et al.*, 2006; *Sparks et al.*, 2009; *Pifko et al.*, 2013]. Although the much reduced detection rate is in part due to the significantly lower sensitivity of SAAMER compared to that of HPLA systems, this is also indicative that the particles producing SAAMER's detected head echoes may be significantly larger than those that contribute to the bulk of the detections by HPLA radars [*Janches et al.*, 2008; *Fentzke et al.*, 2009; *Pifko et al.*, 2013]. First, larger particles will produce larger electron concentrations, so that they may be detected by the lower sensitivity SAAMER system [*Fentzke and Janches*, 2008], and second, the influx rate of meteoroids decreases with increasing size resulting in the lower detected rate [*Ceplecha et al.*, 1998]. In addition, it is worth noting that these observations were performed near the Southern Hemisphere spring equinox, which according to models and observations is the period during which the meteor count rates reach a minimum at a given location [*Janches et al.*, 2006]. This seasonal variability is enhanced, in particular, at higher latitudes [*Sparks et al.*, 2009]. Thus, it is likely the observed rate may increase significantly during the fall equinox period.

Figure 9a presents the initial meteor head echo altitude distribution, that is the altitude at which the first meteor IPP is recorded [*Janches and ReVelle*, 2005]. Although the counts are low, limiting statistical reliability,

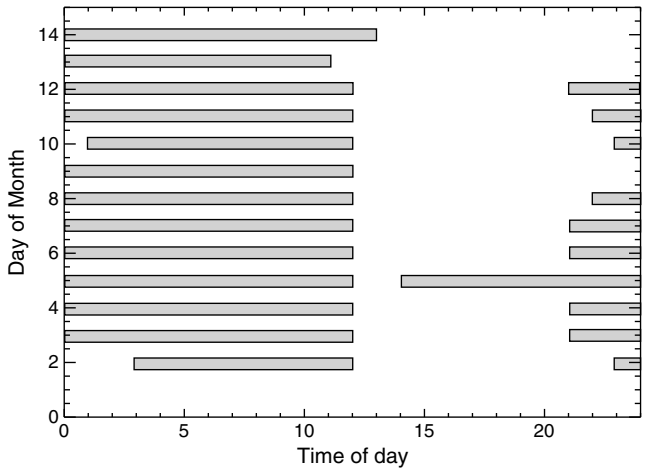

Figure 7. SAAMER's observing periods for the head echo experiment performed in August 2011.

(in particular when compared with HPLA observations), a peak at about ~110 km of altitude is evident from this figure. In addition, more than 45% of SAAMER's detections are between 110 and 120 km. Both the peak and the large percentage of high-altitude events are significantly higher than similar studies utilizing HPLA observations [*Chau and Woodman*, 2004; *Janches et al.*, 2003; *Chau et al.*, 2007; *Sparks et al.*, 2009; *Pifko et al.*, 2013; *Close et al.*, 2012]. One must be cautious when doing these comparisons, however, due to the large

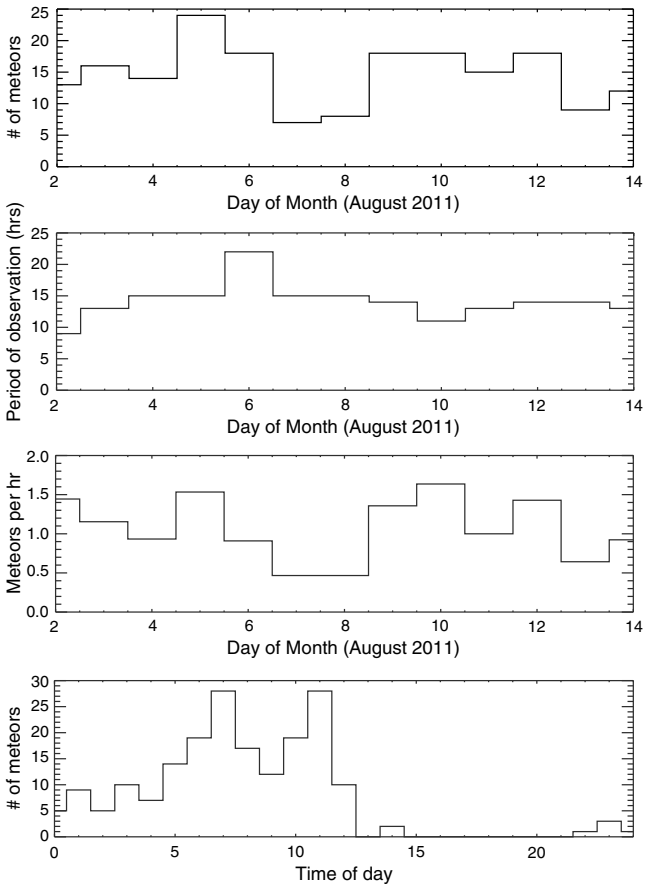

Figure 8. (a) Number of meteors detected per day of observations, (b) number of observed hours per day of observation, (c) average number of meteors per hours observed, and (d) number of meteors observes as a function of time of the day with all days compiled.

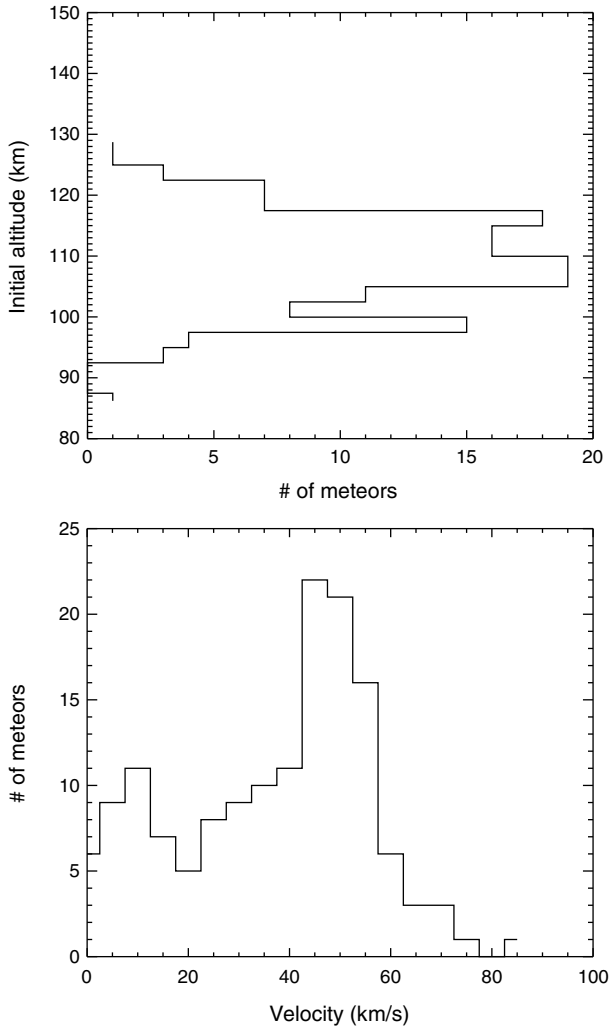

Figure 9. (top) Observed initial altitude distribution and (bottom) observed absolute velocity distribution.

differences in system sensitivity, transmitted frequency, and even detected particle size range. We will discuss this in more detail in the next section.

The geocentric velocity distribution resulting from SAAMER's head echo observations is presented in Figure 9b. Despite the low statistical sample, a clear bimodal distribution shape is evident from this panel, with a dominate peak at 50 km/s and a secondary one at ~11 km/s. The observed higher velocities (≥30 km/s) distribution is generally typical of head echo observations [*Janches et al.*, 2003, 2008; *Sparks et al.*, 2010; *Pifko et al.*, 2013]. Uncertainties of these estimates are obtained by propagating the errors of the individual linear fits (Figure 6). Overall, the methodology presented here provides the absolute velocity estimates with errors of the order of a few to 25%, with only very few cases with higher errors. This is observed in Figure 10 where the distribution of the absolute velocity uncertainty is displayed. The median in this distribution results in 9.7%. Also, Figure 9b shows the presence of a few meteor samples with velocities greater that the solar system escape velocity (i.e., 72 km/s). These particles are also seen in HPLA observations, specially those with interferometric capabilities [*Sato et al.*, 2000; *Chau and Woodman*, 2004; *Chau et al.*, 2007; *Pifko et al.*, 2013]. There are many factors that can produce such detections, such as inaccuracies in the observing methods, acceleration processes due to the giant planets, and indeed true interstellar origin. This issue, however, is currently beyond the scope of this investigation.

The horizontal projections of the vector velocities are displayed in Figure 11. The circles in these figure represent 10° and 20° off zenith at ~110 km of altitude. As can be observed from this figure, most of the detection occurred overhead within 10° off zenith which is the region of higher transmitted power density, with no

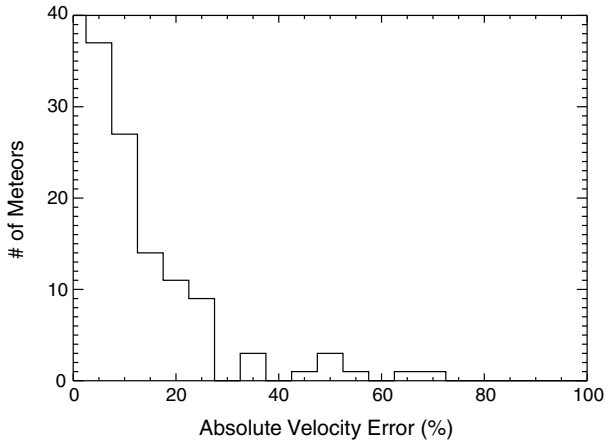

Figure 10. Distribution of calculated errors on the velocity determination.

detections beyond 20° of zenith, from any of the side lobes (Figure 2b). It is important to note that the horizontal projections displayed in Figure 11 are unambiguous meteor positions. This is possible due the use of the five antenna interferometer [*Jones et al.*, 1998]. Furthermore, it can be derived from Figure 11 that most of these observations are relatively long lived, compared to other HPLA observations, with some events producing significant amount of electrons along distances greater than 20 km. This can also be seen in more detail in Figure 12, where distributions of the horizontal, vertical, and absolute distances through which the meteor is observed are displayed. In particular, it can be seen in the third panel of Figure 12 that the majority of observed meteors have typical vertical extents of between half to one atmospheric scale height at those altitudes (~7–10 km). This once again suggests that these meteors are produced by large meteoroids, as will be discussed in the next section.

As a final measured result reported in this section, we present the distribution of the meteor entry angles (i.e., the zenith angle of the meteoroid trajectory) derived from the velocity components. This distribution is displayed in Figure 13. In the figure, an entry angle of 0° corresponds to a trajectory that was aligned with the local vertical (i.e., the meteoroid was traveling straight downward), while 90° corresponds to a horizontal velocity vector. The results in this figure indicate that most of the observations are produced by particles

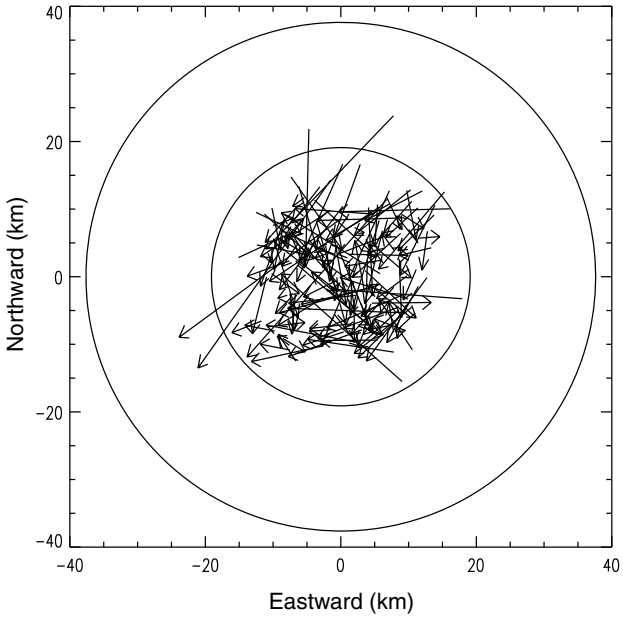

Figure 11. Horizontal projections of the vector velocities displays as arrows. The circles represent 10° and 20° off zenith at 110 km of altitude.

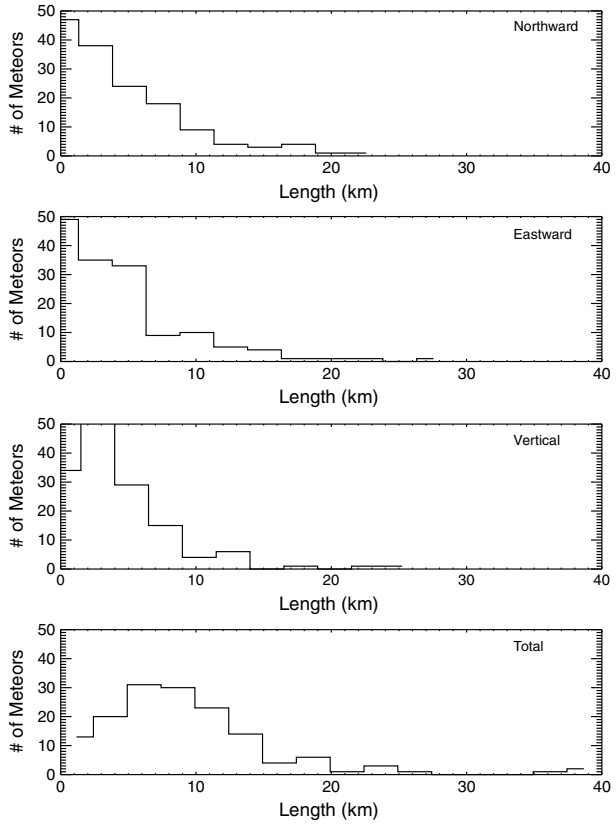

Figure 12. First three panels display the distribution of the spatial coverage of the head echo events in the three directions. The fourth panel displays the distribution of the absolute observed displacement.

entering at angle smaller or equal to 45° with respect to the local zenith. A sharp decrease of meteoroids entering the atmosphere at higher angle values then occurs, and almost no particles with angles higher than ~65°. This observation agrees with past modeling results reported by *Janches et al.* [2006], *Fentzke and Janches* [2008], and *Fentzke et al.* [2009]. In order to obtain agreements between modeled and observed head echo rates by different radars and locations, those authors argued for the need to reject most of the meteoroids entering at these large zenith angles. Recently, *Pifko et al.* [2013] reported interferometric measurements of head echoes using the MU radar in Japan and showed similar results, where the number of

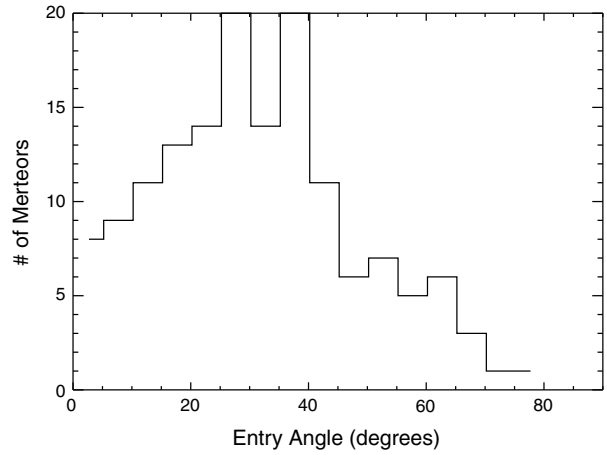

Figure 13. Distribution of calculated entry angle measure from the local zenith.

meteors decrease rapidly for entry angles greater than ~60°, and incoming meteors at angles of ≥75° are, in practical terms, negligible.

5. Discussion

In section 4, we presented a summary of the most representative results and distributions from the head echo observations utilizing SAAMER. In this section we discuss these results in the context of previous head echo observations utilizing HPLA radars and determine how SAAMER's observations compare to and/or complement those obtained with the more powerful and sensitive systems. In section 2, we discussed the difference in beam width between SAAMER's transmitting in Mode 2 and HPLA radars and argued that SAAMER's wider beam will result in sensitivity to larger particles than those generally detected by HPLA radars. We will now attempt to quantify this hypothesis. It is noteworthy that attempts to increase the observation volume of HPLA radars using antenna beam widening has been performed in the past [*Chau et al.*, 2009] to increase the collecting area and consequently increase the likelihood of detecting meteoroids with larger masses. Table 2 presents a comparison of several figures of merit between SAAMER and a selected group of HPLA systems for which meteor head echo observations have been performed and reported repeatedly (column 1). Columns 2 and 3 list the radar operating wavelength and frequency while column 4 provides the peak transmitted power. Note that even though SAAMER is a high-power system when compared to other all-sky meteor radars, it is still 2 orders of magnitude lower than any of the more powerful HPLA radars. Column 5 provides the aperture of each radar. For the case of SAAMER, we calculate its aperture as the area in a circle of diameter equal to 3λ. MU, ALTAIR, and Arecibo are also circular areas with diameters equal to 103, 46, and 300 m, respectively. PFISR and Jicamarca are rectangular areas with dimensions equal to 27.5×31.5 m and 300×300 m, respectively. If we assume that this aperture is the effective aperture, A_{eff}, we can then calculate the Gain (G) as

$$G = 4\pi \frac{A_{\text{eff}}}{\lambda^2} \tag{1}$$

This quantity is listed in column 6. The last column of Table 2 provides the power density (P_d) calculated from

$$P_d = \frac{P_t \times G}{4\pi \times R^2} \tag{2}$$

where R is range chosen to be 110 km for this comparison. We note that, for the case of SAAMER, this may result in an overestimation of its aperture because the array is only sparsely filled, but even if its A_{eff} is reduced to half, it will result in only a 3 dB decrease in G (~7.3 dB), which is comparable to the gain of a single three-element Yagi antenna, and a 1 order of magnitude decrease in P_d. Thus, for the purpose of this discussion, we believe that the results presented in Table 2 are reasonable representations of SAAMER's "best case scenario" performance.

If we utilize P_d as a proxy for the radar sensitivity for the case of head echo observations, the results in Table 2 show that while there is a variability of 3 orders of magnitude of this value among the HPLA systems, SAAMER differs by 4 to 7 orders of magnitude with respect to these sensitive instruments. Thus, while there may be an overlap between the meteoroid mass range detected by each of the HPLA radars, the much smaller sensitivity of SAAMER suggests that the particles producing the head echoes reported here must be significantly larger. Recently, *Pifko et al.* [2013] reported a comparison of detected sensitivity as a function of meteoroid mass between the Arecibo, PFISR, MU, and ALTAIR radars. Utilizing the head echo Radar Cross Section (RCS) model developed by *Close et al.* [2005] combined with the same radar sensitivity approach introduced by *Janches et al.* [2008], the authors estimated the minimum velocity that a meteoroid with a given mass must have to be detected by any of these radars, and the results are reproduced in Table 3. As described by *Close et al.* [2005], the model and, therefore, determined sensitivity are strongly dependent on radar frequency. Taking this into account, we first concentrate on the UHF frequencies by comparing Arecibo and PFISR. Both radars transmit essentially the same frequency (430 and 440 MHz, respectively), have a 2 order of magnitude difference in P_d (Table 2) and 1 order of magnitude difference in meteoroid mass sensitivity (Table 3). That is, PFISR can detect meteoroids traveling at 15 km/s with masses equal to 10 μg, unlike Arecibo, which can detect meteoroids at the same velocity but smaller in mass by an order of magnitude. A similar trend can be observed for VHF frequencies when we compare MU and ALTAIR, although caution must be taken in this case because their frequencies are significantly different. This indicates that, given a

Table 2. Comparison of Various Figures of Merit Between SAAMER and HPLA Radars

RADAR	λ (m)	f (MHz)	P_t (kW)	Aperture (m^2)	G (dB)	P_d (W/m^2)
SAAMER	9.7	32.55	60	74	10	5×10^{-6}
MU	6.5	46	1000	8332.3	34	0.02
Jicamarca	6	50	2000	90,000	45	0.5
ALTAIR	1.8	160	6000	6648	44	1.23
Arecibo	0.69	430	2000	70,686	63	28.9
PFISR	0.68	440	1500	866.25	43	0.3

meteoroid velocity, a difference of 2 orders of magnitude in radar P_d translates to 1 order of magnitude in mass range detected sensitivity. Applying this conjecture to SAAMER and utilizing MU as a reference, since their frequencies are comparable, we can estimate that SAAMER will be able to detect particles with minimum masses of the order of 10^2 μg if the particle travels at very high speeds (~60 km/s) and 10^4 μg if they travel at 15 km/s.

On the other hand, because the number of meteors per unit area per unit time decreases as the particle mass increases [*Ceplecha et al.*, 1998], the maximum mass that each of these radars can detect will be limited by their beam size. For example, *Fentzke and Janches* [2008] and *Fentzke et al.* [2009] determined, using modeling and observed results, that Arecibo's detected mass range, considering all velocities, is 10^{-4} to 10 μg while PFISR's will be 1 to 250 μg. Similarly, *Pifko et al.* [2013] determined a detected mass range by the MU radar of also 1 to 250 μg. This agrees with recent results reported by *Kero et al.* [2011] who, utilizing RCS calculations, determined a MU detected mass range of 1 to 1000 μg. For the case of ALTAIR, *Close et al.* [2012] estimated a detected mass range between 1 to 10^4 μg utilizing an improved technique for calculating bulk densities of low-mass meteoroids using a plasma scattering model. Given the very small collecting area of ALTAIR's VHF system (beam width ~2.8°), it is somewhat surprising to see detection of particles as large as 1000 μg if we assume the mass flux reported by *Ceplecha et al.* [1998] to be correct. However, when looking at the mass distribution in detail, the number of particles decreases abruptly for masses greater than 10^2 μg and values larger than those are simply part of the distribution tail (≤15%; S. Close, personal communication, 2012), which suggests they can be outliers of the model. In any case, it is evident that the minimum masses determined to be detected by SAAMER are equal or greater than the maximum masses detected by HPLA radars as reported by these various authors, and that overall, the SAAMER's head echo detections are produce by larger particles than those which are commonly studied using this technique.

As a final result, we present meteoroid radiant information enabled by the interferometric determination of the vector velocity. Until now, this has only been possible utilizing the ALTAIR, Jicamarca, MU, and PFISR radars [*Sato et al.*, 2000; *Hunt et al.*, 2004; *Chau and Woodman*, 2004; *Chau et al.*, 2007; *Sparks et al.*, 2010; *Kero et al.*, 2011; *Pifko et al.*, 2013]. Figure 14 displays the calculated meteoroid radiant color coded to their velocity plotted in terms of Sun-centered ecliptic longitude ($\lambda - \lambda_0$) and latitude (β). These data represent the point in the sky that the meteoroids entered into a hyperbolic geocentric orbit [*Jones and Brown*, 1993]. The radiant angles are defined such that the ecliptic longitude is the angle of rotation about the ecliptic normal measured from the Earth-Sun direction, and the ecliptic latitude is the angle of rotation out of the ecliptic plane (i.e., the Sun is located at $\lambda - \lambda_0 = 0°$, $\beta = 0°$).

Table 3. Minimum Meteoroid Speed Required for Radar Detection as a Function of Meteoroid Mass for Several HPLA Radar Systems Reproduced From *Pifko et al.* [2013]

Mass ($\log_{10}$ g)	Minimum Speed (km/s)				
	MU	ALTAIR	Arecibo	PFISR	SAAMER
−7	80	40	25	–	–
−6	60	25	15	25	–
−5	25	15	5	15	–
−4	10	All	All	All	60
−3	10	All	All	All	40
−2	All	All	All	All	15

The plots in Figure 14 are oriented such that the center point corresponds to the Apex direction (i.e., the direction of Earth's velocity relative to the Sun). The locations of the six sporadic meteoroid sources are also displayed in the figure as ellipses, with the coordinates as specified in *Pifko et al.* [2013]. The North and South Apex (NA and SA) sources lie just above and below the figure center point, respectively. Likewise, the North and South Toroidal (NT and ST) sources are above and below the respective Apex sources. To the left of the Apex is the Helion (H) direction, and the Anti-Helion (AH) is symmetrically opposite to the

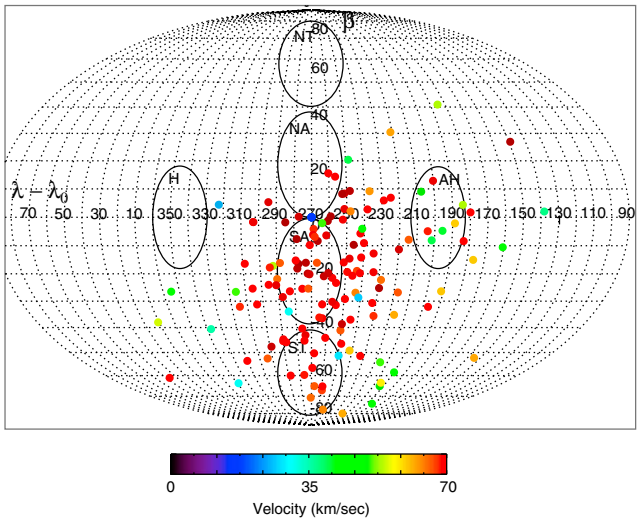

Figure 14. Calculated meteoroid radiant color coded to their velocity plotted in terms of Sun-centered ecliptic longitude ($\lambda - \lambda_0$) and latitude (β). The ellipses represent the location of the six apparent sporadic meteoroid sources.

Helion source about the Apex. As expected given SAAMER's location and the time period during which these observations were performed, the majority of the detections appear to come from the SA and ST source region and a minority originating from the NA and AH regions. Note that most of the radiants lie below 30° in ecliptic latitude, which is expected due to SAAMER's high southern geographical latitude.

6. Conclusions

We have presented meteor head echo observations using SAAMER and demonstrated that, enabled by the enhanced design of this system compared to typical meteor radars, studies that are not based on the commonly detected specular trails are possible. There are many reasons why these results are compelling. Over the past decade, studies of the microgram-size meteoroid mass input in the upper atmosphere have benefited tremendously with the introduction of meteor head echo observations using HPLA radars [*Janches et al.*, 2008]. These observations have enabled us to develop and validate modeling essential for our understanding of the temporal and spatial variability of the meteoric flux, physical characteristics of the meteors and meteoroids, and how they relate to layered phenomena in the Earth's mesopause region [*Janches et al.*, 2006; *Fentzke and Janches*, 2008; *Fentzke et al.*, 2009; *Plane et al.*, 2010; *Gardner et al.*, 2011]. Furthermore, these highly resolved measurements have contributed to identifying the mass loss mechanisms that these particles undergo upon atmospheric entry, allowing us to relate small-scale features of the detected radar light curves with the precise moment that a particular chemical constituent is released from the meteoroid body [*Dyrud and Janches*, 2008; *Janches et al.*, 2009; *Close et al.*, 2012]. The fact that these measurements can be performed only with HPLA radars limits these studies in several ways. First, since HPLA radars are very sensitive instruments with very narrow radar beams, the studies are generally constrained to the lower masses within the spectrum of terrestrial atmospheric aeronomical interest. Second, meteor observations with HPLA radars are scarce because they are made at national observatories, and as such, the allocated observing time on these instruments is shared among many other type of experiments. In fact, only the Arecibo and MU radars have been used extensively to study seasonal effects in the observed meteor diurnal properties [*Kero et al.*, 2011; *Pifko et al.*, 2013; *Janches et al.*, 2006]. The routine utilization of enhanced meteor radars, such as SAAMER, to observe and detect head echoes addresses both issues. First, we have shown that the observational technique can be extended to larger masses, expanding the mass range of particles that can be studied using the same methodology. Second, these systems, even with SAAMER's enhancements, are 2 to 3 orders of magnitude less expensive than HPLA radars, in addition to being easily deployable and almost 100% autonomous. That implies that these observations can be performed continuously and the potential for more deployments at different locations is attainable. This also addresses the low detection rate drawback, since 24 h long observation periods may not provide a statistical significant sample, a problem at this mass range, but because these instruments are operated continuously, the collection

of large data sets over long periods of time is now possible. A methodology to achieve this objective is under current development.

In addition to measurements of the head echo, HPLA radars have been instrumental in the detection and understanding of the plasma phenomena surrounding the nonspecular (i.e., field-aligned) meteor trails [*Dyrud et al.*, 2002, 2007a, 2007b]. Although most of the HPLA radars can be used to detect head echoes, only three (out of 11) [*Janches et al.*, 2008] can successfully detect nonspecular trail echoes, all of which are at low to middle latitudes (ALTAIR in the Marshall Islands, the MU radar in Japan, and the Jicamarca radar in Peru). The characteristics of these echoes (i.e., duration, spatial extend, etc.), which provide key information on meteoroid physical properties [*Dyrud et al.*, 2005], are expected to have a strong dependence with latitude [*Dyrud et al.*, 2011]. Because these echoes are also detected by SAAMER, its location will provide valuable new information regarding this phenomena. These results are under current analysis and will be presented in a future paper.

Finally, over the past decade, there has been a controversy regarding the differences in measured velocity distributions and consequently orbital distributions of meteors resulting from HPLA head echo and meteor radar specular trail detections. These differences are in part due to different observational biases introduced by the detection of different scattering mechanisms using an assorted class of radars. The fact that we can perform measurements of all these mechanisms simultaneously with the same instrument will undoubtedly contribute to clarification of these issues.

Acknowledgments

This work was supported by NSF awards AGS - 0634650, AGS - 0944104, and AST - 0908118, as well as NASA awards 12-PAST12-0007 and 12-PATM12-0006. We wish to thank the EARG personnel for their invaluable help with the operation of SAAMER. The authors wishes to thank M. Nicolls, S. Close, and J. Chau for invaluable discussions.

Robert Lysak thanks Lars Dyrud and two anonymous reviewers for their assistance in evaluating this paper.

References

Baggaley, W. (2002), Radar observations, in *Meteors in the Earth's Atmosphere*, edited by E. Murad and I. Williams, pp. 123–148, Cambridge Univ. Press, Cambridge, U. K.

Brown, P., and J. Jones (1995), A determination of the strengths of the sporadic radio-meteor sources, *Earth Moon and Planets*, *68*, 223–245, doi:10.1007/BF00671512.

Brown, P., R. J. Weryk, D. K. Wong, and J. Jones (2008), The Canadian Meteor Orbit Radar meteor stream catalogue, *Earth Moon and Planets*, *102*, 209–219, doi:10.1007/s11038-007-9162-6.

Campbell-Brown, M. D. (2008a), Directional variation of sporadic meteor activity and velocity, *Earth Moon and Planets*, *102*, 79–84, doi:10.1007/s11038-007-9152-8.

Campbell-Brown, M. D. (2008b), High resolution radiant distribution and orbits of sporadic radar meteoroids, *Icarus*, *196*, 144–163, doi:10.1016/j.icarus.2008.02.022.

Ceplecha, Z., J. Borovička, W. Elford, D. Revelle, R. Hawkes, V. Porubčan, and M. Šimek (1998), Meteor phenomena and bodies, *Space Sci. Rev.*, *84*, 327–471.

Chau, J. L., and R. Woodman (2004), Observations of meteor head-echoes using the Jicamarca 50 MHz radar in interferometer mode, *Atmos. Chem. Phys.*, *3*(6), 6063–6091.

Chau, J. L., R. F. Woodman, and F. Galindo (2007), Sporadic meteor sources as observed by the Jicamarca high-power large-aperture VHF radar, *Icarus*, *188*, 162–174, doi:10.1016/j.icarus.2006.11.006.

Chau, J. L., F. R. Galindo, C. J. Heinselman, and M. J. Nicolls (2009), Meteor-head echo observations using an antenna compression approach with the 450 MHz Poker Flat Incoherent Scatter Radar, *J. Atmos. Sol. Terr. Phys.*, *71*, 636–643, doi:10.1016/j.jastp.2008.08.007.

Close, S., M. Oppenheim, S. Hunt, and A. Coster (2004), A technique for calculating meteor plasma density and meteoroid mass from radar head echo scattering, *Icarus*, *168*, 43–52, doi:10.1016/j.icarus.2003.11.018.

Close, S., M. Oppenheim, D. Durand, and L. Dyrud (2005), A new method for determining meteoroid mass from head echo data, *J. Geophys. Res.*, *110*, A09308, doi:10.1029/2004JA010950.

Close, S., R. Volz, R. Loveland, A. Macdonell, P. Colestock, I. Linscott, and M. Oppenheim (2012), Determining meteoroid bulk densities using a plasma scattering model with high-power large-aperture radar data, *Icarus*, *221*, 300–309, doi:10.1016/j.icarus.2012.07.033.

Close, S., S. M. Hunt, M. J. Minardi, and F. M. McKeen (2000), Analysis of Perseid meteor head echo data collected using the Advance Research Project Agency Long-Range Tracking and Instrumentation Radar (ALTAIR), *Radio Sci.*, *35*(5), 1233–1240.

Currie, T., J. Debes, T. J. Rodigas, A. Burrows, Y. Itoh, M. Fukagawa, S. J. Kenyon, M. Kuchner, and S. Matsumura (2012), Direct imaging confirmation and characterization of a dust-enshrouded candidate exoplanet orbiting Fomalhaut, *Ap. J. Lett.*, *760*, L32, doi:10.1088/2041-8205/760/2/L32.

Dyrud, L., D. Wilson, S. Boerve, J. Trulsen, H. Pecseli, S. Close, C. Chen, and Y. Lee (2007a), Plasma and electromagnetic simulations of meteor head echo radar reflections, *Earth Moon and Planets*, *102*, 383–394, doi:10.1007/s11038-007-9189-8.

Dyrud, L., D. Wilson, S. Boerve, J. Trulsen, H. Pecseli, S. Close, C. Chen, and Y. Lee (2007b), Plasma and electromagnetic wave simulations of meteors, *Adv. Space Res.*, *42*(1), 136–142, doi:10.1016/j.asr.2007.03.048.

Dyrud, L. P., and D. Janches (2008), Modeling the meteor head-echo using Arecibo observations, *J. Atmos. Sol. Terr. Phys.*, *70*, 1621–1632, doi:10.1016/j.jastp.2008.06.016.

Dyrud, L. P., M. M. Oppenheim, S. Close, and S. Hunt (2002), Interpretation of non-specular radar meteor trails, *Geophys. Res. Lett.*, *29*(21), 2012, doi:10.1029/2002GL015953.

Dyrud, L. P., L. Ray, M. Oppenheim, S. Close, and K. Denney (2005), Modelling high-power large-aperture radar meteor trails, *J. Atmos. Terr. Phys.*, *67*, 1171–1177, doi:10.1016/j.jastp.2005.06.016.

Dyrud, L. P., J. Urbina, J. T. Fentzke, E. Hibbit, and J. Hinrichs (2011), Global variation of meteor trail plasma turbulence, *Ann. Geophys.*, *29*, 2277–2286, doi:10.5194/angeo-29-2277-2011.

Evans, J. V. (1965), Radio-echo studies of meteors at 68-centimeter wavelength, *J. Geophys. Res.*, *70*, 5395–5416, doi:10.1029/JZ070i021p05395.

Fentzke, J. T., and D. Janches (2008), A semi-empirical model of the contribution from sporadic meteoroid sources on the meteor input function observed at Arecibo, *J. Geophys. Res.*, *113*, A03304, doi:10.1029/2007JA012531.

Fentzke, J. T., D. Janches, and J. J. Sparks (2009), Latitudinal and seasonal variability of the micrometeor input function: A study using model predictions, Arecibo, and PFISR observations, *J. Atmos. Sol. Terr. Phys.*, *71*, 653–661.

Fritts, D., et al. (2010a), Southern Argentina Agile Meter Radar (SAAMER): System design and initial measurements of large-scale winds and tides, *J. Geophys. Res.*, *115*, D18112, doi:10.1029/2010JD013850.

Fritts, D. C., D. Janches, and W. K. Hocking (2010b), Southern Argentina Agile Meteor Radar: Initial assessment of gravity wave momentum fluxes, *J. Geophys. Res.*, *115*, D19123, doi:10.1029/2010JD013891.

Fritts, D. C., D. Janches, W. K. Hocking, N. J. Mitchell, and M. J. Taylor (2012a), Assessment of gravity wave momentum flux measurement capabilities by meteor radars having different transmitter power and antenna configurations, *J. Geophys. Res.*, *117*, D10108, doi:10.1029/2011JD017174.

Fritts, D. C., D. Janches, H. Iimura, W. K. Hocking, J. V. Bageston, and N. M. P. Leme (2012b), Drake Antarctic Agile Meteor Radar first results: Configuration and comparison of mean and tidal wind and gravity wave momentum flux measurements with Southern Argentina Agile Meteor Radar, *J. Geophys. Res.*, *117*, D02105, doi:10.1029/2011JD016651.

Galligan, D. P., and W. J. Baggaley (2004), The orbital distribution of radar-detected meteoroids of the solar system dust cloud, *Mon. Not. R. Astron. Soc.*, *353*, 422–446, doi:10.1111/j.1365-2966.2004.08078.x.

Galligan, D. P., and W. J. Baggaley (2005), The radiant distribution of AMOR radar meteors, *Mon. Not. R. Astron. Soc.*, *359*, 551–560, doi:10.1111/j.1365-2966.2005.08918.x.

Gardner, C. S., X. Chu, P. Espy, J. Plane, D. Marsh, and D. Janches (2011), Seasonal variations of the mesospheric Fe layer at Rothera, Antarctica, *J. Geophys. Res.*, *116*, D02304, doi:10.1029/2010JD014655.

Hey, J. S., S. J. Parsons, and G. S. Stewart (1947), Radar observations of the Giacobinids meteor shower, 1946, *Mon. Not. R. Astron. Soc.*, *107*, 176.

Hocking, W. K., T. Thayaparan, and J. Jones (1997), Meteor decay times and their use in determining a diagnostic mesospheric temperature-pressure parameter: Methodology and one year of data, *Geophys. Res. Lett.*, *24*, 2977–2980, doi:10.1029/97GL03048.

Hocking, W. K., B. Fueller, and B. Vandepeer (2001), Real-time determination of meteor-related parameters utilizing modern digital technology, *J. Atmos. Sol. Terr. Phys.*, *63*, 155–169.

Hunt, S., M. Oppenheim, S. Close, P. Brown, F. McKeen, and M. Minardi (2004), Determination of the meteoroid velocity distribution at the Earth using high-gain radar, *Icarus*, *168*, 34–42.

Janches, D., and D. ReVelle (2005), The initial altitude of the micrometeor phenomenon: Comparison between Arecibo radar observations and theory, *J. Geophys. Res.*, *110*, A08307, doi:10.1029/2005JA011022.

Janches, D., J. Mathews, D. Meisel, V. Getman, and Q. Zhou (2000a), Doppler studies of near-antapex UHF radar micrometeors, *Icarus*, *143*, 347–353.

Janches, D., J. Mathews, D. Meisel, and Q. Zhou (2000b), Micrometeor observations using the Arecibo 430 MHz radar: I. Determination of the ballistic parameter from measured Doppler velocity and deceleration results, *Icarus*, *145*, 53–63.

Janches, D., A. Pellinen-Wannberg, G. Wannberg, A. Westman, I. Haggsstrom, and D. Meisel (2002), Tristatic observations of meteors using the 930 MHz EISCAT radar system, *J. Geophys. Res.*, *107*(A11), 1389, doi:10.1029/2001JA009205.

Janches, D., M. Nolan, D. Meisel, J. Mathews, Q. Zhou, and D. Moser (2003), On the geocentric micrometeor velocity distribution, *J. Geophys. Res.*, *108*(A6), 1222, doi:10.1029/2002JA009789.

Janches, D., M. Nolan, and M. Sulzer (2004), Radiant measurement accuracy of micrometeors detected by the Arecibo 430 MHz dual-beam radar, *Atmos. Chem. Phys.*, *4*, 621–626.

Janches, D., D. C. Fritts, D. M. Riggin, M. P. Sulzer, and S. Gonzalez (2006), Gravity waves and momentum fluxes in the MLT using 430 MHz dual-beam measurements at Arecibo: 1. Measurements, methods, and gravity waves, *J. Geophys. Res.*, *111*, D18107, doi:10.1029/2005JD006882.

Janches, D., C. Heinselman, J. Chau, A. Chandran, and R. Woodman (2006), Modeling the global micrometeor input function in the upper atmosphere observed by high power and large aperture radars, *J. Geophys. Res.*, *111*, A07317, doi:10.1029/2006JA011628.

Janches, D., S. Close, and J. T. Fentzke (2008), A comparison of detection sensitivity between ALTAIR and Arecibo meteor observations: Can high power and large aperture radars detect low velocity meteor head-echoes, *Icarus*, *193*, 105–111, doi:10.1016/j.icarus.2007.08.022.

Janches, D., L. P. Dyrud, S. L. Broadley, and J. M. C. Plane (2009), First observation of micrometeoroid differential ablation in the atmosphere, *Geophys. Res. Lett.*, *36*, L06101, doi:10.1029/2009GL037389.

Janches, D., J. L. Hormaechea, C. Brunini, W. Hocking, and D. C. Fritts (2013), An initial meteoroid stream survey in the Southern Hemisphere using the Southern Argentina Agile Meteor Radar (SAAMER), *Icarus*, *223*, 677–683, doi:10.1016/j.icarus.2012.12.018.

Johansen, A., J. S. Oishi, M.-M. Mac Low, H. Klahr, T. Henning, and A. Youdin (2007), Rapid planetesimal formation in turbulent circumstellar disks, *Nature*, *448*, 1022–1025, doi:10.1038/nature06086.

Jones, J., and P. Brown (1993), Sporadic meteor radiant distribution: Orbital survey results, *Mon. Not. R. Astron. Soc.*, *265*, 524–532.

Jones, J., A. R. Webster, and W. K. Hocking (1998), An improved interferometer design for use with meteor radars, *Radio Sci.*, *33*, 55–65, doi:10.1029/97RS03050.

Kero, J., C. Szasz, A. Pellinen-Wannberg, G. Wannberg, A. Westman, and D. D. Meisel (2008), Determination of meteoroid physical properties from tristatic radar observations, *Ann. Geophys.*, *26*, 2217–2228, doi:10.5194/angeo-26-2217-2008.

Kero, J., C. Szasz, T. Nakamura, D. D. Meisel, M. Ueda, Y. Fujiwara, T. Terasawa, H. Miyamoto, and K. Nishimura (2011), First results from the 2009–2010 MU radar head echo observation programme for sporadic and shower meteors: The Orionids 2009, *Mon. Not. R. Astron. Soc.*, *416*, 2550–2559, doi:10.1111/j.1365-2966.2011.19146.x.

Kliore, A. J., et al. (2008), First results from the Cassini radio occultations of the Titan ionosphere, *J. Geophys. Res.*, *113*, A09317, doi:10.1029/2007JA012965.

Lau, E. M., S. K. Avery, J. P. Avery, D. Janches, S. E. Palo, R. Schafer, and N. A. Makarov (2006), Statistical characterization of the meteor trail distribution at the South Pole as seen by a VHF interferometric meteor radar, *Radio Sci.*, *41*, RS4007, doi:10.1029/2005RS003247.

Malhotra, R. (1995), The origin of Pluto's orbit: Implications for the solar system beyond Neptune, *Astron. J.*, *110*, 420, doi:10.1086/117532.

Mathews, J. D., D. D. Meisel, K. P. Hunter, V. S. Getman, and Q. Zhou (1997), Very high resolution studies of micrometeors using the Arecibo 430 MHz radar, *Icarus*, *126*, 157–169, doi:10.1006/icar.1996.5641.

Mathews, J. D., D. Janches, D. Meisel, and Q. Zhou (2001), The micrometeoroid mass flux into the upper atmosphere: Arecibo results and a comparison with prior estimates, *Geophys. Res. Lett.*, *28*(10), 1929–1932.

McKinley, D. W. R. (1961), *Meteor Science and Engineering*, pp. 1–309, McGraw Hill, New York.

Nesvorný, D., P. Jenniskens, H. F. Levison, W. F. Bottke, D. Vokrouhlický, and M. Gounelle (2010), Cometary origin of the zodiacal cloud and carbonaceous micrometeorites. Implications for hot debris disks, *Ap. J.*, *713*, 816–836, doi:10.1088/0004-637X/713/2/816.

Nesvorný, D., D. Janches, D. Vokrouhlický, P. Pokorný, W. F. Bottke, and P. Jenniskens (2011a), Dynamical model for the zodiacal cloud and sporadic meteors, *Ap. J.*, *743*, 129, doi:10.1088/0004-637X/743/2/129.

Nesvorný, D., D. Vokrouhlický, P. Pokorný, and D. Janches (2011b), Dynamics of dust particles released from Oort Cloud comets and their contribution to radar meteors, *Ap. J.*, *743*, 37, doi:10.1088/0004-637X/743/1/37.

Okamoto, Y. K., et al. (2004), An early extrasolar planetary system revealed by planetesimal belts in β Pictoris, *Nature*, *431*, 660–663, doi:10.1038/nature02948.

Pätzold, M., S. Tellmann, B. Häusler, D. Hinson, R. Schaa, and G. L. Tyler (2005), A sporadic third layer in the ionosphere of Mars, *Science*, *310*, 837–839, doi:10.1126/science.1117755.

Pätzold, M., S. Tellmann, B. Häusler, M. K. Bird, G. L. Tyler, A. A. Christou, and P. Withers (2009), A sporadic layer in the Venus lower ionosphere of meteoric origin, *Geophys. Res. Lett.*, *36*, L05203, doi:10.1029/2008GL035875.

Pellinen-Wannberg, A., and G. Wannberg (1994), Meteor observations with the European incoherent scatter UHF radar, *J. Geophys. Res.*, *99*, 11,379–11,390, doi:10.1029/94JA00274.

Pifko, S., D. Janches, S. Close, J. Sparks, T. Nakamura, and D. Nesvorny (2013), The meteoroid input function and predictions of mid-latitude meteor observations by the MU radar, *Icarus*, *223*, 444–459, doi:10.1016/j.icarus.2012.12.014.

Plane, J. (2003), Atmospheric chemistry of meteoric metals, *Chem. Rev.*, *103*(12), 4963–4984.

Plane, J., W. Feng, D. Marsh, D. Janches, M. Chipperfield, J. P. Burrows, and M. Sinnhuber (2010), Towards a global model of the meteoric metal layers, *38th COSPAR Scientific Assembly, COSPAR, Plenary Meeting*, vol. 38, p. 1511, Bermen, Germany.

Sato, T., T. Nakamura, and K. Nishimura (2000), Orbit determination of meteors using the MU radar, *IEICE Trans. Commun.*, *E83-B*(9), 1990–1995.

Sparks, J. J., D. Janches, M. J. Nicolls, and C. J. Heinselman (2009), Seasonal and diurnal variability of the meteor flux at high latitudes observed using PFISR, *J. Atmos. Sol. Terr. Phys.*, *71*, 644–652, doi:10.1016/j.jastp.2008.08.009.

Sparks, J. J., D. Janches, M. J. Nicolls, and C. Heinselman (2010), Determination of physical and radiant meteor properties using PFISR interferometry measurements of head echoes, *J. Atmos. Sol. Terr. Phys.*, *72*, 1221–1230, doi:10.1016/j.jastp.2010.08.004.

Walsh, K. J., A. Morbidelli, S. N. Raymond, D. P. O'Brien, and A. M. Mandell (2011), A low mass for Mars from Jupiter's early gas-driven migration, *Nature*, *475*, 206–209, doi:10.1038/nature10201.

Wiegert, P., J. Vaubaillon, and M. Campbell-Brown (2009), A dynamical model of the sporadic meteoroid complex, *Icarus*, *201*, 295–310, doi:10.1016/j.icarus.2008.12.030.

Withers, P., M. Mendillo, D. P. Hinson, and K. Cahoy (2008), Physical characteristics and occurrence rates of meteoric plasma layers detected in the Martian ionosphere by the Mars Global Surveyor Radio Science Experiment, *J. Geophys. Res.*, *113*, A12314, doi:10.1029/2008JA013636.

Younger, J. P., I. M. Reid, R. A. Vincent, D. A. Holdsworth, and D. J. Murphy (2009), A southern hemisphere survey of meteor shower radiants and associated stream orbits using single station radar observations, *Mon. Not. R. Astron. Soc.*, *398*, 350–356, doi:10.1111/j.1365-2966.2009.15142.x.